

Proton-Antiproton Pair Production in Two-Photon Collisions at LEP

The L3 Collaboration

Abstract

The reaction $e^+e^- \rightarrow e^+e^-p\bar{p}$ is studied with the L3 detector at LEP. The analysis is based on data collected at e^+e^- center-of-mass energies from 183 GeV to 209 GeV, corresponding to an integrated luminosity of 667 pb^{-1} . The $\gamma\gamma \rightarrow p\bar{p}$ differential cross section is measured in the range of the two-photon center-of-mass energy from 2.1 GeV to 4.5 GeV. The results are compared to the predictions of the three-quark and quark-diquark models.

Submitted to *Phys. Lett. B*

1 Introduction

Electron-positron colliders are a suitable place for the study of two-photon interactions via the process $e^+e^- \rightarrow e^+e^-\gamma^*\gamma^* \rightarrow e^+e^-X$, where γ^* denotes a virtual photon. The outgoing electron and positron carry almost the full beam energy and are usually undetected, due to their small transverse momenta. The final state X has, therefore, a low mass as compared to the e^+e^- center-of-mass energy, \sqrt{s} , and its transverse momentum is almost zero. The small photon virtuality allows the extraction of the cross section $\sigma(\gamma\gamma \rightarrow X)$ for real photon collisions, once the photon flux is calculated by QED [1].

Calculations of the cross section $\gamma\gamma \rightarrow \text{baryon antibaryon}$ were performed using the hard scattering approach of Brodsky and Lepage [2]. In this formalism, the process is factorized into a perturbative $\gamma\gamma \rightarrow q\bar{q}$ amplitude and a non-perturbative part described by the quark distribution functions of the baryon. Such calculations with three-quark distribution functions [3, 4] yielded results about one order of magnitude below early $\gamma\gamma \rightarrow p\bar{p}$ measurements [5] for $\gamma\gamma$ center-of-mass energies, $W_{\gamma\gamma}$, less than 3 GeV. The quark-diquark model [6] was proposed as a possible way to model non-perturbative effects. Within this model, the partonic structure of the baryon is described by a quark-diquark system rather than three quarks. The composite nature of diquarks is taken into account by form factors ensuring that the three-quark model is recovered at an asymptotically large momentum transfer.

This Letter presents a study of the differential cross section of the reaction $\gamma\gamma \rightarrow p\bar{p}$ in the $W_{\gamma\gamma}$ range from 2.1 GeV to 4.5 GeV. The data sample corresponds to a total integrated luminosity of 667 pb^{-1} collected with the L3 detector [7] at $\sqrt{s} = 183 - 209 \text{ GeV}$. The analysis is based on the central tracking system and the high resolution BGO electromagnetic calorimeter. The events are selected by the track triggers [8].

The $p\bar{p}$ final state in two-photon collisions was previously studied at lower \sqrt{s} [5, 9] and recently at LEP [10] with lower statistics. The present study extends the $W_{\gamma\gamma}$ range. Our results are compared to these experiments and to recent theoretical predictions of the quark-diquark model [11].

2 Monte Carlo simulation

Monte Carlo events for the $\gamma\gamma \rightarrow p\bar{p}$ reaction, as well as for the background processes $\gamma\gamma \rightarrow K^+K^-$ and $\gamma\gamma \rightarrow \pi^+\pi^-$, are generated with the PC Monte Carlo program [12], for each beam energy, within the formalism of Reference 1. The $e^+e^- \rightarrow e^+e^-\tau^+\tau^-$, $e^+e^- \rightarrow e^+e^-\mu^+\mu^-$ and $e^+e^- \rightarrow e^+e^-e^+e^-$ background processes are simulated with the DIAG36 [13] generator which includes the full set of $\mathcal{O}(\alpha^4)$ QED diagrams. The generated events are passed through the full L3 detector simulation using the GEANT [14] and GEISHA [15] programs and are reconstructed with the same programs as the data. Time dependent detector inefficiencies, as monitored during the data taking period, are taken into account.

3 Proton-antiproton event selection

In order to match the experimental acceptance with the range of the theoretical predictions, the data are analysed only in the region $|\cos\theta^*| < 0.6$, where θ^* is the center-of-mass production angle of the proton. Events are first selected by requiring two well-reconstructed tracks of opposite charge. The track selection criteria are:

- a distance of closest approach to the interaction point less than 3 mm in the plane transverse to the beam direction,
- at least 30 hits, out of a maximum of 62, in the tracking chamber,
- a matched energy cluster in the electromagnetic calorimeter,
- a transverse momentum, p_t , greater than 400 MeV, to ensure a high trigger efficiency and electron rejection.

The identification of $\gamma\gamma \rightarrow p\bar{p}$ events is mainly based on three artificial neural networks, used to separate antiprotons from e^- , μ^- and h^- , where h^- represents either a π^- or K^- . Each neural network consists of five input nodes, a single layer of five hidden neurons and one output neuron. The following measured quantities are associated with the five input nodes:

- the momentum of the antiproton,
- the probability for the proton mass hypothesis based on the mean energy loss dE/dx measured in the tracker,
- the ratio E_t/p_t , where E_t is the transverse energy measured in the electromagnetic calorimeter,
- the number of BGO crystals in the calorimetric cluster associated with the antiproton,
- the ratio between the energy deposited in the central crystal of the cluster and the sum of the energies deposited in the three-by-three matrix of crystals around it.

The two last variables exploit the typical signature of an antiproton annihilating in the BGO electromagnetic calorimeter: a broad shower spanning several crystals, as opposed to narrow showers for electrons, minimum ionisation deposition for muons and compact showers for low energy hadrons. Each neural network is trained with the corresponding sample from Monte Carlo simulations so that its output value is close to one for antiprotons.

A particle is identified as an antiproton after a cut on the output of the three neural networks. The efficiency for antiproton detection is found to be 74%. Even though the e^- neural network rejects more than 98% of the electrons, the $e^+e^- \rightarrow e^+e^-e^+e^-$ cross section is more than two orders of magnitude greater than the $e^+e^- \rightarrow e^+e^-p\bar{p}$ cross section and the electron contamination still remains important. To reduce this background, the ratio E_t/p_t of the proton candidate is required to be less than 0.6, as shown in Figure 1. In addition, the confidence level that the dE/dx measurement is consistent with a proton must be more than 5%. These cuts eliminate more than 95% of the remaining $e^+e^- \rightarrow e^+e^-e^+e^-$ background.

4 Exclusive $\gamma\gamma \rightarrow p\bar{p}$ event selection

To select exclusive $\gamma\gamma \rightarrow p\bar{p}$ events the following further cuts are applied:

- Events with a photon candidate outside a cone of 36 degrees half-opening angle with respect to the antiproton direction are rejected. A photon candidate is defined as a shower in the electromagnetic calorimeter with at least two adjacent crystals, an energy greater than 100 MeV and no charged tracks within a cone of 200 mrad half-opening angle.

- The square of the total transverse momentum of the proton-antiproton pair $(\sum \vec{p}_t)^2$ must be less than 0.1 GeV^2 . This cut reduces inclusive background events of the type $e^+e^- \rightarrow e^+e^-p\bar{p}X$, where X represents one or more unobserved particles.

These cuts yield a total number of 989 selected events. Figure 2 shows the distribution of the effective mass of the $p\bar{p}$ pair, identified with $W_{\gamma\gamma}$. It is obtained by assigning the proton mass to the two tracks.

The exclusive background is estimated by processing the corresponding Monte Carlo events with the same analysis cuts. The $\gamma\gamma \rightarrow \pi^+\pi^-$ and $\gamma\gamma \rightarrow K^+K^-$ cross sections given in Reference 16 are used. This background is found to be negligible in the region $W_{\gamma\gamma} < 2.5 \text{ GeV}$ and increases up to 25% above 2.5 GeV. The $e^+e^- \rightarrow e^+e^-e^+e^-$ background varies from 5% in the low mass region to 30% in the high mass region. The $e^+e^- \rightarrow e^+e^-\mu^+\mu^-$ contamination is less than 0.2% and neglected. The contamination of inclusive channels and of $e^+e^- \rightarrow e^+e^-\tau^+\tau^-$ is estimated by fitting the tail of the $(\sum \vec{p}_t)^2$ distribution. The extrapolation to the region $(\sum \vec{p}_t)^2 < 0.1 \text{ GeV}^2$ gives an average background level of $(2 \pm 1)\%$. The sum of all backgrounds is subtracted bin by bin for the cross section determination. The background composition of each bin is detailed in Table 1.

5 Cross section measurements

The detection efficiency is determined by Monte Carlo simulation in bins of $W_{\gamma\gamma}$ and $|\cos\theta^*|$. It takes into account the track acceptance and selection criteria, the exclusive proton-antiproton identification criteria and the track trigger efficiency. This trigger efficiency is 91% at $W_{\gamma\gamma} = 2.1 \text{ GeV}$ and rises to 98% for $W_{\gamma\gamma} > 3 \text{ GeV}$. The higher level trigger efficiencies are estimated from the data themselves, using prescaled events, and range from 88% at $W_{\gamma\gamma} = 2.1 \text{ GeV}$ up to 99% for $W_{\gamma\gamma} > 3 \text{ GeV}$. The total selection efficiency is found to be maximum, about 6%, at $W_{\gamma\gamma} \simeq 2.5 \text{ GeV}$ and $|\cos\theta^*| < 0.1$. It decreases both at larger $|\cos\theta^*|$ and $W_{\gamma\gamma}$, due respectively to limited angular acceptance and antiproton identification efficiency. The average efficiencies as a function of $W_{\gamma\gamma}$ for $|\cos\theta^*| < 0.6$ and as a function of $|\cos\theta^*|$ for $W_{\gamma\gamma} < 4.5 \text{ GeV}$ are presented in Figure 3.

The cross sections are evaluated in bins of $W_{\gamma\gamma}$ and $|\cos\theta^*|$ for different values of \sqrt{s} . Due to the limited selection efficiency near threshold (Figure 3), the measurement is restricted to the range $W_{\gamma\gamma} > 2.1 \text{ GeV}$. A total of 938 events are selected after this cut. The differential cross sections are integrated to obtain the production cross sections $e^+e^- \rightarrow e^+e^-p\bar{p}$ for $|\cos\theta^*| < 0.6$ and $2.1 \text{ GeV} < W_{\gamma\gamma} < 4.5 \text{ GeV}$ as a function of \sqrt{s} . Since the results show no significant \sqrt{s} dependence they are combined into a single measurement at $\langle\sqrt{s}\rangle = 197 \text{ GeV}$:

$$\sigma(e^+e^- \rightarrow e^+e^-p\bar{p}) = 26.7 \pm 0.9 \pm 2.7 \text{ pb}$$

where the first uncertainty is statistical, the second systematic.

The following systematic uncertainties are considered. The uncertainty due to the selection procedure is evaluated by varying the selection cuts. The uncertainty on the neural network outputs is estimated by varying the input variables according to their resolution. An uncertainty of 50% on the $\gamma\gamma \rightarrow \pi^+\pi^-$ and $\gamma\gamma \rightarrow K^+K^-$ cross sections is propagated in the background subtraction. The uncertainty on the $e^+e^- \rightarrow e^+e^-e^+e^-$ background is estimated to be 30%. The uncertainty of 50% on the level of inclusive background is also included. For low values of $W_{\gamma\gamma}$ the dominant systematic uncertainty is about 7% and is due to selection cut variation. It

remains the most important systematic uncertainty for $W_{\gamma\gamma} < 3.2$ GeV, as large as 30%. For $W_{\gamma\gamma} > 3.2$ GeV, the background subtraction uncertainty becomes the most important, rising to 55% in the last $W_{\gamma\gamma}$ bin. The systematic uncertainties shown in Table 2 are the quadratic sum of the different sources.

The differential cross section $d\sigma(\gamma\gamma \rightarrow p\bar{p})/d|\cos\theta^*|$ for real photon-photon collisions is extracted as a function of $W_{\gamma\gamma}$ by dividing out the two-photon luminosity function and extrapolating to $Q^2 = 0$ with a GVDM form factor [17]. The luminosity functions are evaluated for each \sqrt{s} and $W_{\gamma\gamma}$ interval. The measured differential cross sections are integrated to obtain the cross sections $\sigma(\gamma\gamma \rightarrow p\bar{p})$. An additional uncertainty of 5%, due to the choice of the photon form factor, is included in the systematics. The results are reported in Table 2. The present measurement is of higher statistical precision and extends towards higher values of $W_{\gamma\gamma}$ than the previous results [5, 9, 10]. Agreement is observed within the quoted uncertainties, except for the measurements of Reference 10 which lie below our data in the low mass region.

6 Discussion of the results

The results are compared to the predictions of the three-quark [3] and the recent quark-diquark model [11] in Figure 4. The three-quark prediction is based on the leading order QCD calculations, using the distribution function of Chernyak and Zhitnisky [18]. The quark-diquark calculation is performed with the standard proton distribution amplitudes [11] and includes first order corrections due to the non-vanishing proton mass. While the shapes of the theoretical curves are quite similar, the normalisations are significantly different. The predictions of the three-quark model are about an order of magnitude below the measurement, whereas the quark-diquark predictions describe the data much better. The apparent change in the logarithmic slope of the cross section observed in data at $W_{\gamma\gamma}$ around 3 GeV is, however, not reproduced by this model.

In order to investigate this further, the differential cross sections are summed separately in three mass intervals: $2.1 \text{ GeV} < W_{\gamma\gamma} < 2.5 \text{ GeV}$, $2.5 \text{ GeV} < W_{\gamma\gamma} < 3.0 \text{ GeV}$ and $3.0 \text{ GeV} < W_{\gamma\gamma} < 4.5 \text{ GeV}$. The results are reported in Table 3 and plotted in Figure 5. A distinctive difference between the three distributions can be observed. No prediction is available for the diquark model for $W_{\gamma\gamma} < 2.5$ GeV, but it can be seen that the data has a qualitatively different behaviour to the diquark predictions, as it is strongly peaked at large angles. Assuming the presence of a single angular momentum state in the s -channel of $\gamma\gamma \rightarrow p\bar{p}$ production, a fit to a single spherical harmonic: Y_0^0 , Y_2^0 , Y_2^1 or Y_2^2 is performed. This does not give a satisfactory result. An acceptable fit is obtained using all of them, but only the Y_2^0 contribution is significantly different from zero. A satisfactory fit is also obtained using only the Y_0^0 and Y_2^0 harmonics with the fractions 8% and 92% respectively, as shown in Figure 5a. The intermediate region exhibits a rather flat dependence, which partially agrees with the model predictions. The forward peaking behaviour of the differential cross section in the high mass interval is well reproduced by the quark-diquark model. Only in this region, then, the data can be described by the Brodsky-Lepage hard scattering approach.

The presence of two distinct production mechanisms can also be seen in Figure 6a and Table 4 by considering separately the cross sections as a function of $W_{\gamma\gamma}$ in a large angle region, $|\cos\theta^*| < 0.3$, and in a region $0.3 < |\cos\theta^*| < 0.6$. The shape of the efficiency as a function of $W_{\gamma\gamma}$ is similar for the two regions. The large angle cross section dominates in the low mass region and shows a steeper fall-off with $W_{\gamma\gamma}$ than the small angle cross section. A fit of the form $\sigma(W) \propto W^{-n}$ to the small angle region shown in Figure 6b gives a reasonably good

description with $n = 9.8 \pm 0.3$. The data are also in agreement with the quark-diquark model prediction in this region. On the other hand, Figure 6c, the large angle cross section cannot be described by a simple power law behaviour for $W_{\gamma\gamma}$ less than 3 GeV and does not follow the quark-diquark prediction. In this case, the change of shape at 3 GeV is similar to, but more pronounced than that in Figure 4.

In conclusion, an accurate study of the $\gamma\gamma \rightarrow p\bar{p}$ process is performed. The present results are of higher statistical precision and extend towards higher values of $W_{\gamma\gamma}$ than those of previous experiments. Current models are only moderately successful in describing the observed data. These data can provide useful inputs for predictions of other $\gamma\gamma \rightarrow \text{baryon antibaryon}$ channels [19].

References

- [1] V. M. Budnev *et al.*, Phys. Rep. **15** (1974) 181.
- [2] S. J. Brodsky and J. P. Lepage, Phys. Rev. **D 22** (1980) 2157.
- [3] G. Farrar, E. Maina and F. Neri, Nucl. Phys. **B 259** (1985) 702; Nucl. Phys. **B 263** (1986) 746.
- [4] D. Millers and J. F. Gunion, Phys. Rev. **D 34** (1986) 2657.
- [5] TASSO, M. Althoff *et al.*, Phys. Lett. **B 130** (1983) 449;
JADE, W. Bartel *et al.*, Phys. Lett. **B 174** (1986) 350;
TPC/ 2γ , H. Aihara *et al.*, Phys. Rev. **D 56** (1987) 3506;
ARGUS, H. Albrecht *et al.*, Z. Phys. **C 42** (1989) 543.
- [6] M. Anselmino *et al.*, Int. Jour. Mod. Phys. **A 4** (1989) 5213.
- [7] L3 Collab., B. Adeva *et al.*, Nucl. Instr. Meth. **A 289** (1990) 35;
L3 Collab., O. Adriani *et al.*, Phys. Rep. **236** (1993) 1;
M. Chemarin *et al.*, Nucl. Instr. Meth. **A 349** (1994) 345;
M. Acciarri *et al.*, Nucl. Instr. Meth. **A 351** (1994) 300;
I. C. Brock *et al.*, Nucl. Instr. Meth. **A 381** (1996) 236;
A. Adam *et al.*, Nucl. Instr. Meth. **A 383** (1996) 342.
- [8] P. Béné *et al.*, Nucl. Inst. Meth. **A 306** (1991) 150;
D. Haas *et al.*, Nucl. Inst. Meth. **A 420** (1991) 101.
- [9] CLEO, M. Artuso *et al.*, Phys. Rev. **D 50** (1994) 5484;
VENUS, H. Hamasaki *et al.*, Phys. Lett. **B 407** (1997) 185.
- [10] OPAL Collab., G. Abbiendi *et al.*, preprint hep-ex/0209052 (2002).
- [11] C. F. Berger, B. Lechner and W. Schweiger, Fizika **B 8** (1999) 371;
C. F. Berger and W. Schweiger, preprint hep-ph/0212066 (2002).
We thank C. F. Berger and W. Schweiger for providing us with their model predictions.
- [12] F. L. Linde, *Charm Production in Two-Photon Collisions*, Ph.D. Thesis, Rijksuniversiteit Leiden, 1988.
- [13] DIAG36, F. A. Berends, P. H. Daverfeldt and R. Kleiss, Nucl. Phys. **B 253** (1985) 441.
- [14] GEANT version 3.21, R. Brun *et al.*, CERN report CERN DD/EE/84-1 (1984), revised 1987.
- [15] GEISHA, H. Fesefeldt, RWTH Aachen report PITHA 85/2 (1985).
- [16] K. Gzrelak, in *Proceedings of the International Conference on the Structure and Interactions of the Photon* (Photon 2001), Eds. M. N. Kienzle and M. Wadhwa (World Scientific, Singapore, 2001).
- [17] G. A. Schuler, preprint hep-ph/9610406 (1986).

- [18] V. L. Chernyak and I. R. Zhitnitsky, Nucl. Phys. **B 246** (1984) 52.
- [19] M. Diehl, P. Kroll and C. Vogt, Eur. Phys. J. **C 26** (2003) 567.

The L3 Collaboration:

P.Achard,²⁰ O.Adriani,¹⁷ M.Aguilar-Benitez,²⁴ J.Alcaraz,²⁴ G.Alemanni,²² J.Allaby,¹⁸ A.Aloisio,²⁸ M.G.Alvigi,²⁸ H.Anderhub,⁴⁶ V.P.Andreev,^{6,33} F.Anselmo,⁸ A.Arefiev,²⁷ T.Azmoon,³ T.Aziz,⁹ P.Bagnaia,³⁸ A.Bajo,²⁴ G.Baksay,²⁵ L.Baksay,²⁵ S.V.Baldew,² S.Banerjee,⁹ Sw.Banerjee,⁴ A.Barczyk,^{46,44} R.Barillere,¹⁸ P.Bartalini,²² M.Basile,⁸ N.Batalova,⁴³ R.Battiston,³² A.Bay,²² F.Becattini,¹⁷ U.Becker,¹³ F.Behner,⁴⁶ L.Bellucci,¹⁷ R.Berbeco,³ J.Berdugo,²⁴ P.Berges,¹³ B.Bertucci,³² B.L.Betev,⁴⁶ M.Biasini,³² M.Biglietti,²⁸ A.Biland,⁴⁶ J.J.Blaising,⁴ S.C.Blyth,³⁴ G.J.Bobbink,² A.Böhm,¹ L.Boldizsar,¹² B.Borgia,³⁸ S.Bottai,¹⁷ D.Bourilkov,⁴⁶ M.Bourquin,²⁰ S.Braccini,²⁰ J.G.Branson,⁴⁰ F.Brochu,⁴ J.D.Burger,¹³ W.J.Burger,³² X.D.Cai,¹³ M.Capell,¹³ G.Cara Romeo,⁸ G.Carlinio,²⁸ A.Cartacci,¹⁷ J.Casaus,²⁴ F.Cavallari,³⁸ N.Cavallo,³⁵ C.Cecchi,³² M.Cerrada,²⁴ M.Chamizo,²⁰ Y.H.Chang,⁴⁸ M.Chemarin,²³ A.Chen,⁴⁸ G.Chen,⁷ G.M.Chen,⁷ H.F.Chen,²¹ H.S.Chen,⁷ G.Chiefari,²⁸ L.Cifarelli,³⁹ F.Cindolo,⁸ I.Clare,¹³ R.Clare,³⁷ G.Coignet,⁴ N.Colino,²⁴ S.Costantini,³⁸ B.de la Cruz,²⁴ S.Cucciarelli,³² J.A.van Dalen,³⁰ R.de Asmundis,²⁸ P.Déglon,²⁰ J.Debreczeni,¹² A.Degré,⁴ K.Dehmelt,²⁵ K.Deiters,⁴⁴ D.della Volpe,²⁸ E.Delmeire,²⁰ P.Denes,³⁶ F.DeNotaristefani,³⁸ A.De Salvo,⁴⁶ M.Diemoz,³⁸ M.Dierckxsens,² C.Dionisi,³⁸ M.Dittmar,⁴⁶ A.Doria,²⁸ M.T.Dova,^{10,‡} D.Duchesneau,⁴ M.Duda,¹ B.Echenard,²⁰ A.Eline,¹⁸ A.El Hage,¹ H.El Mamouni,²³ A.Engler,³⁴ F.J.Eppling,¹³ P.Extermann,²⁰ M.A.Falagan,²⁴ S.Falciano,³⁸ A.Favara,³¹ J.Fay,²³ O.Fedin,³³ M.Felcini,⁴⁶ T.Ferguson,³⁴ H.Fesefeldt,¹ E.Fiandrini,³² J.H.Field,²⁰ F.Filthaut,³⁰ P.H.Fisher,¹³ W.Fisher,³⁶ I.Fisk,⁴⁰ G.Forconi,¹³ K.Freudenreich,⁴⁶ C.Furetta,²⁶ Yu.Galaktionov,^{27,13} S.N.Ganguli,⁹ P.Garcia-Abia,²⁴ M.Gataullin,³¹ S.Gentile,³⁸ S.Giagu,³⁸ Z.F.Gong,²¹ G.Grenier,²³ O.Grimm,⁴⁶ M.W.Gruenewald,¹⁶ M.Guida,³⁹ R.van Gulik,² V.K.Gupta,³⁶ A.Gurtu,⁹ L.J.Gutay,⁴³ D.Haas,⁵ R.Sh.Hakobyan,³⁰ D.Hatzifotiadou,⁸ T.Hebbeker,¹ A.Hervé,¹⁸ J.Hirschfelder,³⁴ H.Hofer,⁴⁶ M.Hohlmann,²⁵ G.Holzner,⁴⁶ S.R.Hou,⁴⁸ Y.Hu,³⁰ B.N.Jin,⁷ L.W.Jones,³ P.de Jong,² I.Josa-Mutuberría,²⁴ D.Käfer,¹ M.Kaur,¹⁴ M.N.Kienzle-Focacci,²⁰ J.K.Kim,⁴² J.Kirkby,¹⁸ W.Kittel,³⁰ A.Klimentov,^{13,27} A.C.König,³⁰ M.Kopal,⁴³ V.Koutsenko,^{13,27} M.Kräber,⁴⁶ R.W.Kraemer,³⁴ A.Krüger,⁴⁵ A.Kunin,¹³ P.Ladron de Guevara,²⁴ I.Laktineh,²³ G.Landi,¹⁷ M.Lebeau,¹⁸ A.Lebedev,¹³ P.Lebrun,²³ P.Lecomte,⁴⁶ P.Lecoq,¹⁸ P.Le Coultre,⁴⁶ J.M.Le Goff,¹⁸ R.Leiste,⁴⁵ M.Levtchenko,²⁶ P.Levtchenko,³³ C.Li,²¹ S.Likhoded,⁴⁵ C.H.Lin,⁴⁸ W.T.Lin,⁴⁸ F.L.Linde,² L.Lista,²⁸ Z.A.Liu,⁷ W.Lohmann,⁴⁵ E.Longo,³⁸ Y.S.Lu,⁷ C.Luci,³⁸ L.Luminari,³⁸ W.Lustermann,⁴⁶ W.G.Ma,²¹ L.Malgeri,²⁰ A.Malinin,²⁷ C.Maña,²⁴ J.Mans,³⁶ J.P.Martin,²³ F.Marzano,³⁸ K.Mazumdar,⁹ R.R.McNeil,⁶ S.Mele,^{18,28} L.Merola,²⁸ M.Meschini,¹⁷ W.J.Metzger,³⁰ A.Mihul,¹¹ H.Milcent,¹⁸ G.Mirabelli,³⁸ J.Mnich,¹ G.B.Mohanty,⁹ G.S.Muanza,²³ A.J.M.Muijs,² B.Musicar,⁴⁰ M.Musy,³⁸ S.Nagy,¹⁵ S.Natale,²⁰ M.Napolitano,²⁸ F.Nessi-Tedaldi,⁴⁶ H.Newman,³¹ A.Nisati,³⁸ H.Nowak,⁴⁵ R.Ofierzynski,⁴⁶ G.Organtini,³⁸ I.Pal,⁴³ C.Palomares,²⁴ P.Paolucci,²⁸ R.Paramatti,³⁸ G.Passaleva,¹⁷ S.Patricelli,²⁸ T.Paul,¹⁰ M.Pauluzzi,³² C.Paus,¹³ F.Pauss,⁴⁶ M.Pedace,³⁸ S.Pensotti,²⁶ D.Perret-Gallix,⁴ B.Petersen,³⁰ D.Piccolo,²⁸ F.Pierella,⁸ M.Pioppi,³² P.A.Piroué,³⁶ E.Pistolesi,²⁶ V.Plyaskin,²⁷ M.Pohl,²⁰ V.Pojidaev,¹⁷ J.Pothier,¹⁸ D.Prokofiev,³³ J.Quartieri,³⁹ G.Rahal-Callot,⁴⁶ M.A.Rahaman,⁹ P.Raics,¹⁵ N.Raja,⁹ R.Ramelli,⁴⁶ P.G.Rancoita,²⁶ R.Ranieri,¹⁷ A.Raspereza,⁴⁵ P.Razis,²⁹ D.Ren,⁴⁶ M.Rescigno,³⁸ S.Reucroft,¹⁰ S.Riemann,⁴⁵ K.Riles,³ B.P.Roe,³ L.Romero,²⁴ A.Rosca,⁴⁵ S.Rosier-Lees,⁴ S.Roth,¹ C.Rosenbleck,¹ J.A.Rubio,¹⁸ G.Ruggiero,¹⁷ H.Rykaczewski,⁴⁶ A.Sakharov,⁴⁶ S.Saremi,⁶ S.Sarkar,³⁸ J.Salicio,¹⁸ E.Sanchez,²⁴ C.Schäfer,¹⁸ V.Schegelsky,³³ H.Schopper,⁴⁷ D.J.Schotanus,³⁰ C.Sciacca,²⁸ L.Servoli,³² S.Shevchenko,³¹ N.Shivarov,⁴¹ V.Shoutko,¹³ E.Shumilov,²⁷ A.Shvorob,³¹ D.Son,⁴² C.Souga,²³ P.Spillantini,¹⁷ M.Steuer,¹³ D.P.Stickland,³⁶ B.Stoyanov,⁴¹ A.Straessner,¹⁸ K.Sudhakar,⁹ G.Sultanov,⁴¹ L.Z.Sun,²¹ S.Sushkov,¹ H.Suter,⁴⁶ J.D.Swain,¹⁰ Z.Szillasi,^{25,¶} X.W.Tang,⁷ P.Tarjan,¹⁵ L.Tauscher,⁵ L.Taylor,¹⁰ B.Tellili,²³ D.Teyssier,²³ C.Timmermans,³⁰ Samuel C.C.Ting,¹³ S.M.Ting,¹³ S.C.Tonwar,⁹ J.Tóth,¹² C.Tully,³⁶ K.L.Tung,⁷ J.Ulbricht,⁴⁶ E.Valente,³⁸ R.T.Van de Walle,³⁰ R.Vasquez,⁴³ V.Veszpremi,²⁵ G.Vesztergombi,¹² I.Vetlitsky,²⁷ D.Vicinanza,³⁹ G.Viertel,⁴⁶ S.Villa,³⁷ M.Vivargent,⁴ S.Vlachos,⁵ I.Vodopianov,²⁵ H.Vogel,³⁴ H.Vogt,⁴⁵ I.Vorobiev,^{34,27} A.A.Vorobyov,³³ M.Wadhwa,⁵ Q.Wang,³⁰ X.L.Wang,²¹ Z.M.Wang,²¹ M.Weber,¹ P.Wienemann,¹ H.Wilkens,³⁰ S.Wynhoff,³⁶ L.Xia,³¹ Z.Z.Xu,²¹ J.Yamamoto,³ B.Z.Yang,²¹ C.G.Yang,⁷ H.J.Yang,³ M.Yang,⁷ S.C.Yeh,⁴⁹ An.Zalite,³³ Yu.Zalite,³³ Z.P.Zhang,²¹ J.Zhao,²¹ G.Y.Zhu,⁷ R.Y.Zhu,³¹ H.L.Zhuang,⁷ A.Zichichi,^{8,18,19} B.Zimmermann,⁴⁶ M.Zöller,¹

- 1 III. Physikalisches Institut, RWTH, D-52056 Aachen, Germany[§]
 - 2 National Institute for High Energy Physics, NIKHEF, and University of Amsterdam, NL-1009 DB Amsterdam, The Netherlands
 - 3 University of Michigan, Ann Arbor, MI 48109, USA
 - 4 Laboratoire d'Annecy-le-Vieux de Physique des Particules, LAPP,IN2P3-CNRS, BP 110, F-74941 Annecy-le-Vieux CEDEX, France
 - 5 Institute of Physics, University of Basel, CH-4056 Basel, Switzerland
 - 6 Louisiana State University, Baton Rouge, LA 70803, USA
 - 7 Institute of High Energy Physics, IHEP, 100039 Beijing, China[△]
 - 8 University of Bologna and INFN-Sezione di Bologna, I-40126 Bologna, Italy
 - 9 Tata Institute of Fundamental Research, Mumbai (Bombay) 400 005, India
 - 10 Northeastern University, Boston, MA 02115, USA
 - 11 Institute of Atomic Physics and University of Bucharest, R-76900 Bucharest, Romania
 - 12 Central Research Institute for Physics of the Hungarian Academy of Sciences, H-1525 Budapest 114, Hungary[‡]
 - 13 Massachusetts Institute of Technology, Cambridge, MA 02139, USA
 - 14 Panjab University, Chandigarh 160 014, India.
 - 15 KLTE-ATOMKI, H-4010 Debrecen, Hungary[¶]
 - 16 Department of Experimental Physics, University College Dublin, Belfield, Dublin 4, Ireland
 - 17 INFN Sezione di Firenze and University of Florence, I-50125 Florence, Italy
 - 18 European Laboratory for Particle Physics, CERN, CH-1211 Geneva 23, Switzerland
 - 19 World Laboratory, FBLJA Project, CH-1211 Geneva 23, Switzerland
 - 20 University of Geneva, CH-1211 Geneva 4, Switzerland
 - 21 Chinese University of Science and Technology, USTC, Hefei, Anhui 230 029, China[△]
 - 22 University of Lausanne, CH-1015 Lausanne, Switzerland
 - 23 Institut de Physique Nucléaire de Lyon, IN2P3-CNRS, Université Claude Bernard, F-69622 Villeurbanne, France
 - 24 Centro de Investigaciones Energéticas, Medioambientales y Tecnológicas, CIEMAT, E-28040 Madrid, Spain^b
 - 25 Florida Institute of Technology, Melbourne, FL 32901, USA
 - 26 INFN-Sezione di Milano, I-20133 Milan, Italy
 - 27 Institute of Theoretical and Experimental Physics, ITEP, Moscow, Russia
 - 28 INFN-Sezione di Napoli and University of Naples, I-80125 Naples, Italy
 - 29 Department of Physics, University of Cyprus, Nicosia, Cyprus
 - 30 University of Nijmegen and NIKHEF, NL-6525 ED Nijmegen, The Netherlands
 - 31 California Institute of Technology, Pasadena, CA 91125, USA
 - 32 INFN-Sezione di Perugia and Università Degli Studi di Perugia, I-06100 Perugia, Italy
 - 33 Nuclear Physics Institute, St. Petersburg, Russia
 - 34 Carnegie Mellon University, Pittsburgh, PA 15213, USA
 - 35 INFN-Sezione di Napoli and University of Potenza, I-85100 Potenza, Italy
 - 36 Princeton University, Princeton, NJ 08544, USA
 - 37 University of California, Riverside, CA 92521, USA
 - 38 INFN-Sezione di Roma and University of Rome, "La Sapienza", I-00185 Rome, Italy
 - 39 University and INFN, Salerno, I-84100 Salerno, Italy
 - 40 University of California, San Diego, CA 92093, USA
 - 41 Bulgarian Academy of Sciences, Central Lab. of Mechatronics and Instrumentation, BU-1113 Sofia, Bulgaria
 - 42 The Center for High Energy Physics, Kyungpook National University, 702-701 Taegu, Republic of Korea
 - 43 Purdue University, West Lafayette, IN 47907, USA
 - 44 Paul Scherrer Institut, PSI, CH-5232 Villigen, Switzerland
 - 45 DESY, D-15738 Zeuthen, Germany
 - 46 Eidgenössische Technische Hochschule, ETH Zürich, CH-8093 Zürich, Switzerland
 - 47 University of Hamburg, D-22761 Hamburg, Germany
 - 48 National Central University, Chung-Li, Taiwan, China
 - 49 Department of Physics, National Tsing Hua University, Taiwan, China
- § Supported by the German Bundesministerium für Bildung, Wissenschaft, Forschung und Technologie
- ‡ Supported by the Hungarian OTKA fund under contract numbers T019181, F023259 and T037350.
- ¶ Also supported by the Hungarian OTKA fund under contract number T026178.
- ^b Supported also by the Comisión Interministerial de Ciencia y Tecnología.
- [‡] Also supported by CONICET and Universidad Nacional de La Plata, CC 67, 1900 La Plata, Argentina.
- △ Supported by the National Natural Science Foundation of China.

$W_{\gamma\gamma}$ (GeV)	inclusive (%)	e^+e^- (%)	h^+h^- (%)
2.1 – 2.2	1	3	<1
2.2 – 2.3	1	4	<1
2.3 – 2.4	1	6	<1
2.4 – 2.5	1	8	<1
2.5 – 2.6	2	12	3
2.6 – 2.8	3	18	5
2.8 – 3.2	7	29	17
3.2 – 3.6	12	24	21
3.6 – 4.5	18	26	25

Table 1: The estimated inclusive, e^+e^- and h^+h^- backgrounds in each $W_{\gamma\gamma}$ bin.

$W_{\gamma\gamma}$ (GeV)	$\langle W_{\gamma\gamma} \rangle$ (GeV)	Number of Events	Background (%)	$\sigma(\gamma\gamma \rightarrow p\bar{p})$ (nb)
2.1 – 2.2	2.15	216	4	$5.35 \pm 0.36 \pm 0.55$
2.2 – 2.3	2.25	252	5	$4.34 \pm 0.27 \pm 0.41$
2.3 – 2.4	2.35	182	7	$2.86 \pm 0.21 \pm 0.28$
2.4 – 2.5	2.45	111	10	$1.78 \pm 0.17 \pm 0.18$
2.5 – 2.6	2.55	61	16	$1.01 \pm 0.13 \pm 0.11$
2.6 – 2.8	2.69	57	25	$0.50 \pm 0.07 \pm 0.09$
2.8 – 3.2	2.97	32	54	$0.12 \pm 0.02 \pm 0.05$
3.2 – 3.6	3.37	15	57	$0.06 \pm 0.02 \pm 0.03$
3.6 – 4.5	3.95	12	69	$0.02 \pm 0.01 \pm 0.01$

Table 2: The number of events, estimated background and $\gamma\gamma \rightarrow p\bar{p}$ cross section as a function of $W_{\gamma\gamma}$ for $|\cos\theta^*| < 0.6$. The average value $\langle W_{\gamma\gamma} \rangle$ of each bin corresponds to a weighted average according to a $W_{\gamma\gamma}^{-12}$ distribution. The first uncertainty is statistical, the second systematic.

$ \cos\theta^* $	$d\sigma(\gamma\gamma \rightarrow p\bar{p})/d \cos\theta^* $ (nb)		
	$2.1 \text{ GeV} < W_{\gamma\gamma} < 2.5 \text{ GeV}$	$2.5 \text{ GeV} < W_{\gamma\gamma} < 3.0 \text{ GeV}$	$3.0 \text{ GeV} < W_{\gamma\gamma} < 4.5 \text{ GeV}$
0 – 0.1	$10.36 \pm 0.64 \pm 1.08$	$0.86 \pm 0.16 \pm 0.14$	$0.06 \pm 0.02 \pm 0.03$
0.1 – 0.2	$7.79 \pm 0.57 \pm 0.81$	$0.56 \pm 0.12 \pm 0.09$	$0.04 \pm 0.02 \pm 0.02$
0.2 – 0.3	$6.15 \pm 0.53 \pm 0.64$	$0.62 \pm 0.14 \pm 0.10$	$0.03 \pm 0.02 \pm 0.02$
0.3 – 0.4	$5.39 \pm 0.54 \pm 0.56$	$1.01 \pm 0.18 \pm 0.17$	$0.06 \pm 0.02 \pm 0.03$
0.4 – 0.5	$3.77 \pm 0.50 \pm 0.39$	$0.82 \pm 0.18 \pm 0.14$	$0.07 \pm 0.03 \pm 0.04$
0.5 – 0.6	$2.30 \pm 0.48 \pm 0.24$	$1.03 \pm 0.22 \pm 0.17$	$0.11 \pm 0.04 \pm 0.05$

Table 3: The differential cross section as a function of $|\cos\theta^*|$ for the different $W_{\gamma\gamma}$ ranges. The first uncertainty is statistical, the second systematic.

$W_{\gamma\gamma}$ (GeV)	$\langle W_{\gamma\gamma} \rangle$ (GeV)	$\sigma(\gamma\gamma \rightarrow p\bar{p})$ (nb)	
		$ \cos\theta^* < 0.3$	$0.3 < \cos\theta^* < 0.6$
2.1 – 2.2	2.15	$(3.58 \pm 0.27 \pm 0.37)$	$(1.78 \pm 0.27 \pm 0.18)$
2.2 – 2.3	2.25	$(2.95 \pm 0.21 \pm 0.28)$	$(1.40 \pm 0.18 \pm 0.13)$
2.3 – 2.4	2.35	$(2.01 \pm 0.17 \pm 0.19)$	$(0.85 \pm 0.13 \pm 0.08)$
2.4 – 2.5	2.45	$(1.21 \pm 0.13 \pm 0.12)$	$(0.57 \pm 0.11 \pm 0.06)$
2.5 – 2.6	2.55	$(0.54 \pm 0.09 \pm 0.06)$	$(0.47 \pm 0.09 \pm 0.05)$
2.6 – 2.8	2.69	$(0.19 \pm 0.04 \pm 0.03)$	$(0.31 \pm 0.06 \pm 0.05)$
2.8 – 3.2	2.97	$(0.03 \pm 0.01 \pm 0.01)$	$(0.09 \pm 0.02 \pm 0.04)$
3.2 – 3.6	3.37	$(0.02 \pm 0.01 \pm 0.01)$	$(0.04 \pm 0.01 \pm 0.02)$
3.6 – 4.5	3.95	$(10 \pm 4 \pm 6) \times 10^{-3}$	$(11 \pm 5 \pm 7) \times 10^{-3}$

Table 4: $\gamma\gamma \rightarrow p\bar{p}$ cross section as a function of $W_{\gamma\gamma}$ for $|\cos\theta^*| < 0.3$ and $0.3 < |\cos\theta^*| < 0.6$. The average value $\langle W_{\gamma\gamma} \rangle$ of each bin corresponds to a weighted average according to a $W_{\gamma\gamma}^{-12}$ distribution. The first uncertainty is statistical, the second systematic.

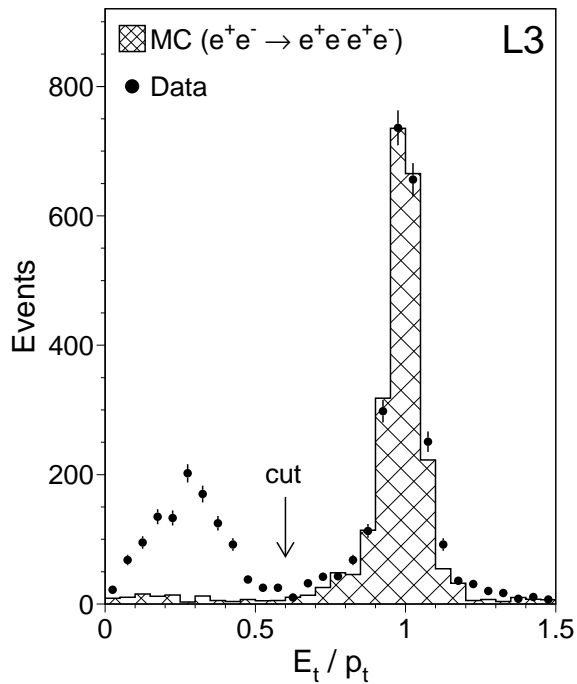


Figure 1: The ratio between the transverse energy deposited in the electromagnetic calorimeter, E_t , and the transverse momentum, p_t , for the proton candidate after the antiproton selection. The $e^+e^- \rightarrow e^+e^-e^+e^-$ Monte Carlo prediction is superimposed on the data.

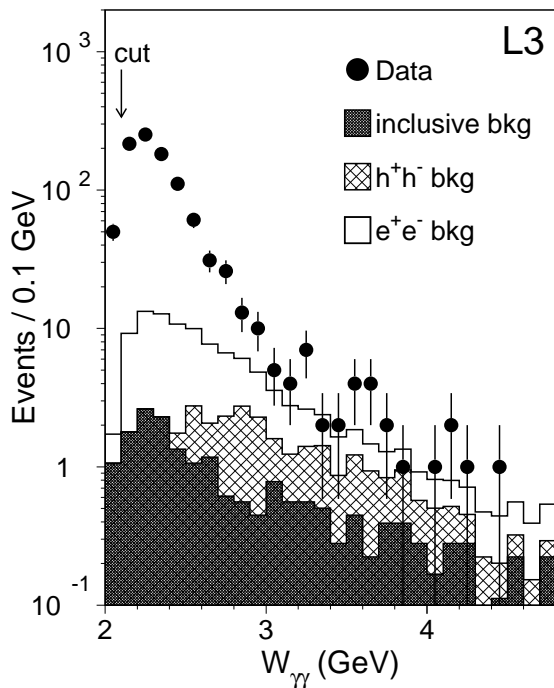


Figure 2: The effective mass of the $p\bar{p}$ pair, $W_{\gamma\gamma}$, for the 989 selected events. The 938 events at the right of the cut are used in the subsequent analysis.

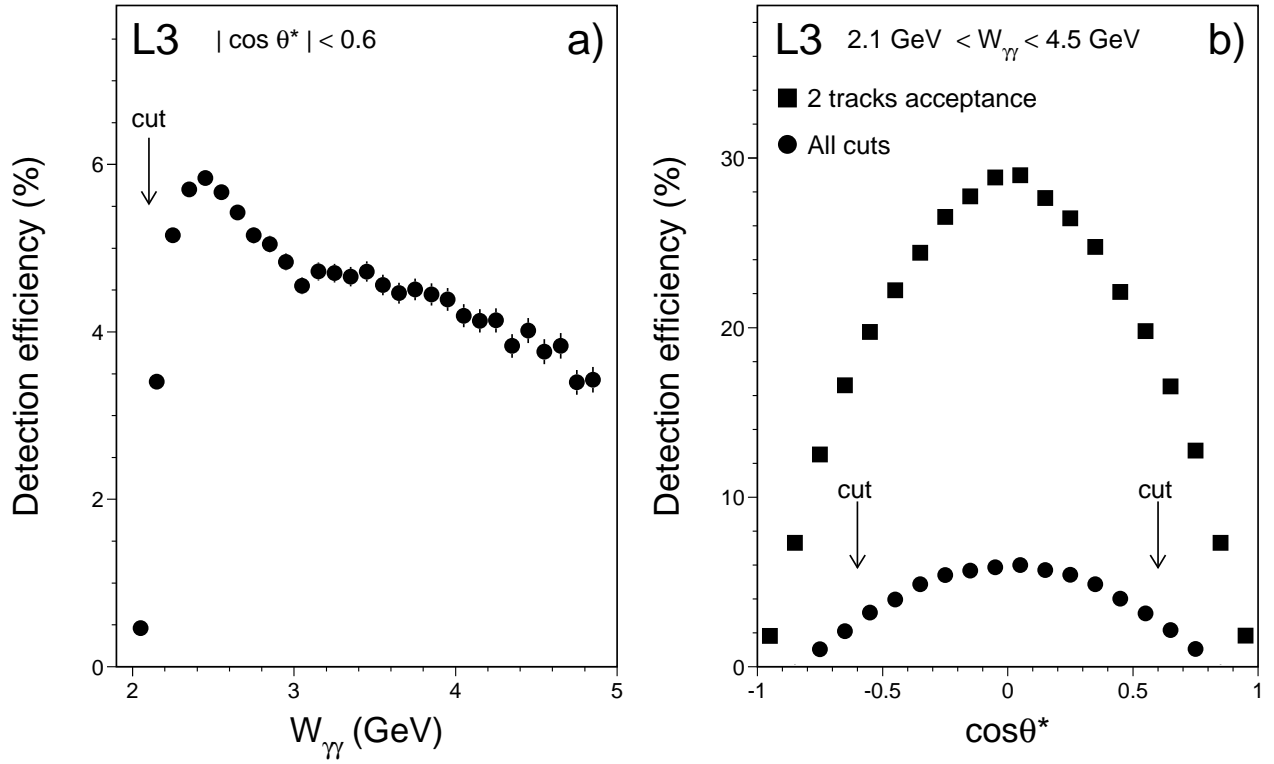


Figure 3: The selection efficiency as a function of a) $W_{\gamma\gamma}$ for $|\cos\theta^*| < 0.6$ and b) $\cos\theta^*$ (full circles) for $2.1 \text{ GeV} < W_{\gamma\gamma} < 4.5 \text{ GeV}$. The full squares indicate the efficiency for detecting two charged tracks of opposite charge in the detector, with no further requirements.

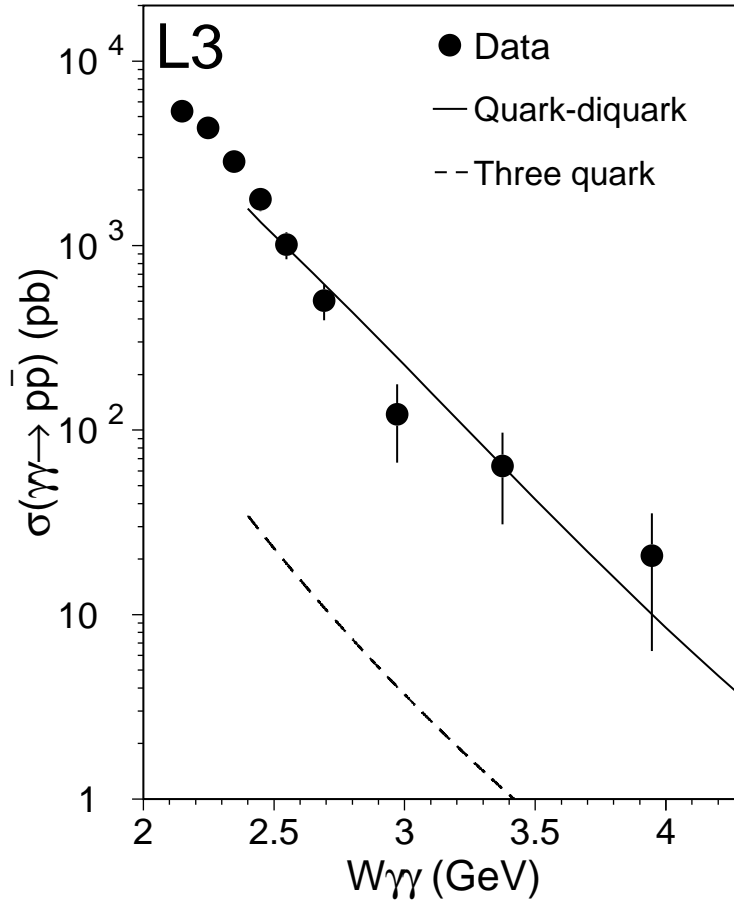


Figure 4: The $\gamma\gamma \rightarrow p\bar{p}$ cross sections as a function of $W_{\gamma\gamma}$ for $|\cos\theta^*| < 0.6$ compared to the three-quark model calculation [3] and to the recent quark-diquark model prediction [11], available for $W_{\gamma\gamma} > 2.5$ GeV. Statistical and systematic uncertainties are added in quadrature.

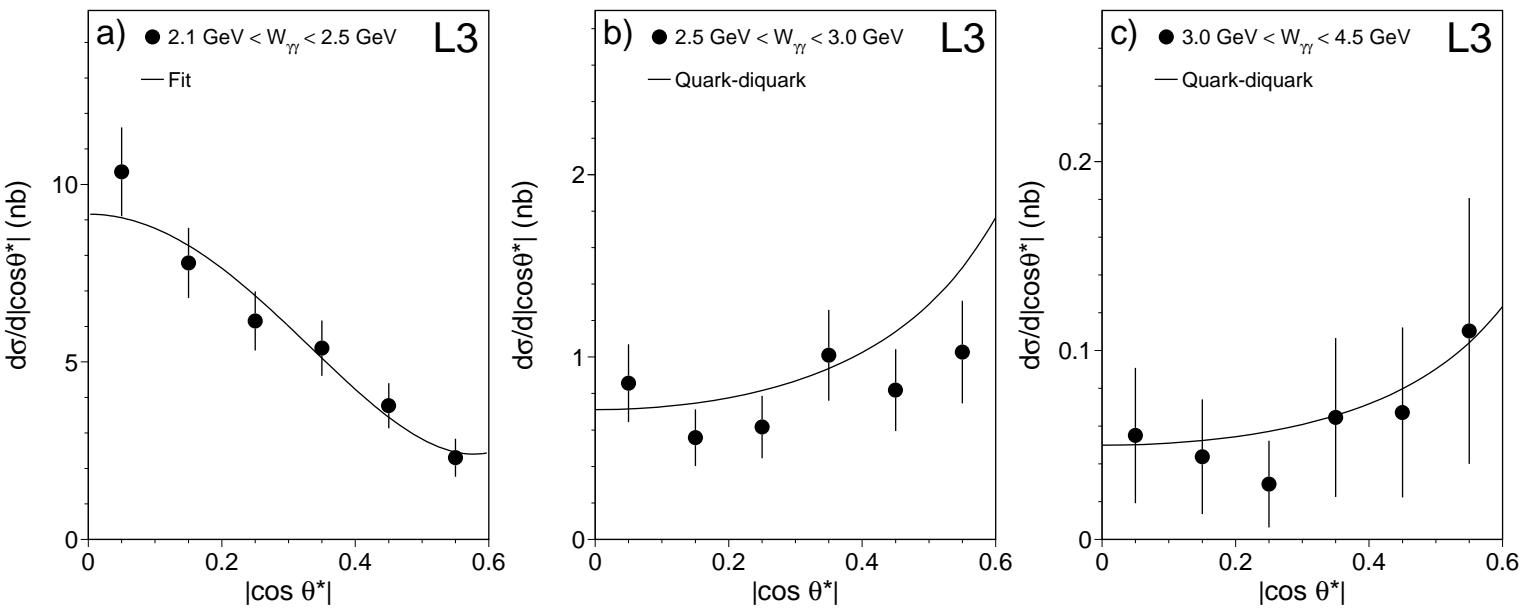


Figure 5: The differential cross section as a function of $|\cos \theta^*|$ for a) $2.1 < W_{\gamma\gamma} < 2.5 \text{ GeV}$, b) $2.5 < W_{\gamma\gamma} < 3.0 \text{ GeV}$ and c) $3.0 < W_{\gamma\gamma} < 4.5 \text{ GeV}$. The data are compared to the predictions of the quark-diquark model. The fit in a) is described in the text.

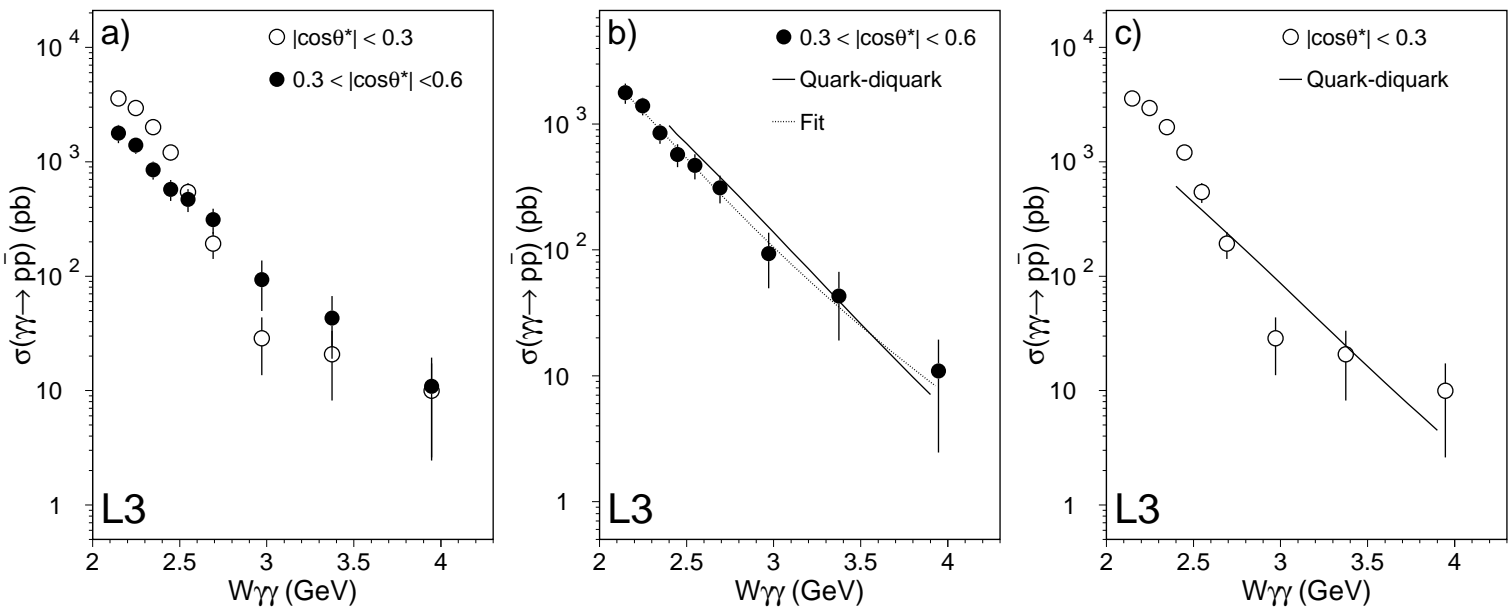


Figure 6: a) The $\gamma\gamma \rightarrow p\bar{p}$ cross section as a function of $W_{\gamma\gamma}$ for the large angle region, $|\cos\theta^*| < 0.3$ (full circle), and the small angle region, $0.3 < |\cos\theta^*| < 0.6$ (open circle). b) The small angle and c) the large angle cross section with the quark-diquark model predictions and the fit described in text.